Acta Pharmaceutica Sinica B 2026;16(6):3784−3801

Chinese Pharmaceutical Association
Institute of Materia Medica, Chinese Academy of Medical Sciences

Acta Pharmaceutica Sinica B

www.elsevier.com/locate/apsb
www.sciencedirect.com

ORIGINAL ARTICLE

# VPS34 inhibition as a host-targeting anti-coronaviral strategy: Rational design of YBM with optimized pharmacokinetic parameters

**Chenchen Ge[a,†], Zihao Wang[b,†], Zhiwei Zhao[c], Xiaoyu Zhang[a], Xiaoyang Yu[a], Minghua Chen[a], Kai Liu[a], Lisen Lin[a], Dapeng Li[a], Ningyi Jin[a], Peifu Jiao[b], Shiyong Fan[b,*], Chao Shang[a,*], Xiao Li[a,*]**

[a]*Changchun Veterinary Research Institute, Chinese Academy of Agricultural Sciences, Changchun 130122, China*
[b]*National Engineering Research Center for the Emergency Drug, Beijing Institute of Pharmacology and Toxicology, Beijing 100850, China*
[c]*College of Life Sciences, Shandong Normal University, Jinan 250014, China*

Received 25 July 2025; received in revised form 16 October 2025; accepted 17 November 2025

**KEY WORDS**

Host-targeting antivirals;
Broad-spectrum anti-coronavirus;
SARS-CoV-2;
HCoV-OC43;
VPS34;
*In vivo*;
Pharmacokinetics;
Inhibitors

**Abstract** Targeting host factors critical to the viral life cycle instead of direct viral enzyme inhibition represents a promising alternative strategy for developing broad-spectrum antivirals. Here, we identified VPS34, a key regulator of autophagosome−lysosome fusion and membrane trafficking, as a conserved host-dependency factor across coronaviruses. *VPS34* gene knockdown significantly attenuates viral replication both *in vitro* and *in vivo*. Crucially, this antiviral effect remained potent against emerging severe acute respiratory syndrome coronavirus 2 (SARS-CoV-2) variants, demonstrating that VPS34 is a drug target resilient to viral evolution. Based on the scaffold structure of the VPS34 inhibitor SAR405, we developed YBM, a novel small-molecule inhibitor, *via* critical group substitutions and aliphatic chain introduction. YBM exhibited superior pharmacokinetic properties than SAR405, including enhanced bioavailability and prolonged plasma half-life. YBM shows significant *in vivo* efficacy against SARS-CoV-2 and HCoV-OC43. Crucially, its broad-spectrum potential is underscored by potent *in vitro* activity against multiple coronavirus genera ($\alpha$ and $\gamma$). This study established YBM as a host-targeting antiviral (HTA) that targets VPS34, offering protection against both extant and evolving coronaviruses. The evolutionarily conserved role of VPS34 in mediating coronavirus replication suggests that this host factor may become a priority therapeutic target for coronaviruses during future pandemics.

*Corresponding authors.
E-mail addresses: fansy@bmi.ac.cn (Shiyong Fan), shangchao1290@126.com (Chao Shang), skylee6226@163.com (Xiao Li).
[†]These authors made equal contributions to this work.

Peer review under the responsibility of Chinese Pharmaceutical Association and Institute of Materia Medica, Chinese Academy of Medical Sciences.

https://doi.org/10.1016/j.apsb.2025.12.020

## 1. Introduction

The coronavirus disease (COVID-19) pandemic has inflicted profound socioeconomic disruption on human society, resulting in millions of deaths and substantial morbidity globally. As of the latest epidemiological updates, SARS-CoV-2 continues to circulate with emerging variants such as JN.1, maintaining its pandemic potential in multiple regions[1]. By April 2025, the WHO has reported 776.9 million confirmed cases and 7 million deaths worldwide, though Institute for Health Metrics and Evaluation estimates suggest that actual mortality may be 2.74-fold higher than reported figures[2−6]. The FDA has approved three antiviral agents for COVID-19 therapy, including two RNA-dependent RNA polymerase inhibitors (remdesivir and molnupiravir) and one main protease (Mpro) inhibitor (nirmatrelvir). Nirmatrelvir is co-administered with ritonavir as Paxlovid™ to enhance pharmacokinetic properties through CYP3A4 inhibition[7]. Despite the clinical efficacy of Paxlovid™, potent CYP3A4 inhibition by ritonavir raises significant drug−drug interaction risks, potentially causing severe adverse events. Growing evidence indicates that SARS-CoV-2 can develop resistance mutations against direct-acting antivirals (DAAs), diminishing antiviral efficacy by up to 288-fold[8-10]. This vulnerability is underscored by emerging clinical reports, including: remdesivir resistance mutation identified during treatment of persistent SARS-CoV-2 infection, Paxlovid™ resistant variants detected in treated patients[11,12]. DAAs impose strong selective pressure on viruses. Combined with the high mutation rate inherent to RNA viral replication, this accelerates target site mutations in viral genomes, thus compromising therapeutic efficacy. These limitations underscore the urgent need for host-directed therapeutics targeting conserved coronavirus−host interactions to achieve broad-spectrum antiviral activity and mitigate resistance development. Host-targeting antivirals (HTAs) exhibit distinct therapeutic advantages over DAAs. By targeting evolutionarily conserved host-dependency factors essential for viral replication, HTAs achieve broad-spectrum antiviral coverage across related viral families[13,14]. This mechanism enables HTAs to maintain efficacy against emerging viral variants that develop resistance to DAAs through mutations in viral enzymes. Moreover, host organisms exhibit significantly lower genetic variability and mutation rates than viruses.

Viral replication complexes are associated with host intracellular membranes for all positive-stranded RNA viruses studied to date, although the origins and nature of these membranes vary[15]. Virus-induced double-membrane vesicles (DMVs) exhibit striking structural similarities to autophagosomes, suggesting that viruses exploit autophagy or the components involved in autophagosome formation to generate viral replication organelles. $\beta$-Coronaviruses remodel host intracellular membranes into DMVs for genome replication and transcription. VPS34, a unique member of the class III phosphatidylinositol 3-kinase (PI3K) family, is highly conserved in mammals and yeast, and critically involved in biological functions and disease pathogenesis[16]. VPS34 complex 1 (Beclin1−VPS34−ATG14) facilitates autophagosome formation during autophagy initiation, whereas VPS34 complex 2 (Beclin1−VPS34−UVRAG) promotes autophagosome−lysosome fusion during autophagosome maturation[17]. As a key autophagy regulator, VPS34 participates in SARS-CoV-2 DMV biogenesis, and treatment with the VPS34 inhibitor PIK-III reduces the number of NSP3−NSP4−NSP5-induced DMVs[18]. We have previously demonstrated that autophagy induction facilitates SARS-CoV-2 infection, while administration of the VPS34 inhibitor 3-MA suppresses viral replication in both xenografted human lung and hACE2-transgenic mouse models[19]. Thus, we propose that VPS34 is a critical host factor essential for coronavirus replication. However, a systematic investigation of its therapeutic efficacy and pan-coronaviral activity as a broad-spectrum drug target is lacking, with no comprehensive studies validating its cross-coronavirus applicability reported to date.

The therapeutic efficacy of antiviral drugs is partially determined by their tissue distribution and metabolism after systemic absorption. Suboptimal pharmacokinetic (PK) properties are an inherent limitation of many antivirals and remain a key focus in antiviral drug development[20]. Although several highly specific and selective VPS34 inhibitors have been identified through screening campaigns, most have only been tested in animal models of cancer and no studies have evaluated VPS34 inhibitors for antiviral applications *in vivo*[21]. This gap holds particular significance owing to the fundamentally distinct PK profiles required for antiviral and anticancer therapies. A prime example is SARS-CoV-2, for which therapeutic success demands optimized pulmonary bioavailability, metabolic stability, and pharmacological properties that are markedly different from those prioritized in oncology drug development. Thus, more effective VPS34 inhibitors should be developed to validate their antiviral efficacy *in vivo* and assess their clinical potential.

In this study, we employed *VPS34* gene knockdown in both cellular and animal models to comprehensively evaluate its utility as an HTA target both *in vitro* and *in vivo*. However, the existing VPS34 inhibitors have demonstrated suboptimal *in vivo* efficacy against coronaviruses. Thus, we performed structure−activity relationship-guided structural modifications of SAR405, a known VPS34 inhibitor, to comprehensively enhance its PK profile and improve tissue distribution. The optimized compound demonstrated potent antiviral efficacy *in vivo*, conferring full protection against a lethal SARS-CoV-2 challenge in mice.

## 2. Materials and methods

### 2.1. Cells, animals, and viruses

Human kidney epithelial cell-derived HEK293-hACE2 and African green monkey kidney Vero E6 cells were maintained in Dulbecco's modified Eagle's medium (DMEM) containing 1% penicillin−streptomycin and 10% FBS (Gibco). Lung-specific VPS34-deficient (*Vps34*$^{flox/+}$ *Sftpc cre*) and *Vps34*$^{flox/+}$ mice were purchased from Cyagen Biosciences (Suzhou, China). Female BALB/c mice (8−9 months old) were purchased from Beijing Vital River Laboratory Animal Technology Co., Ltd. The SARS-

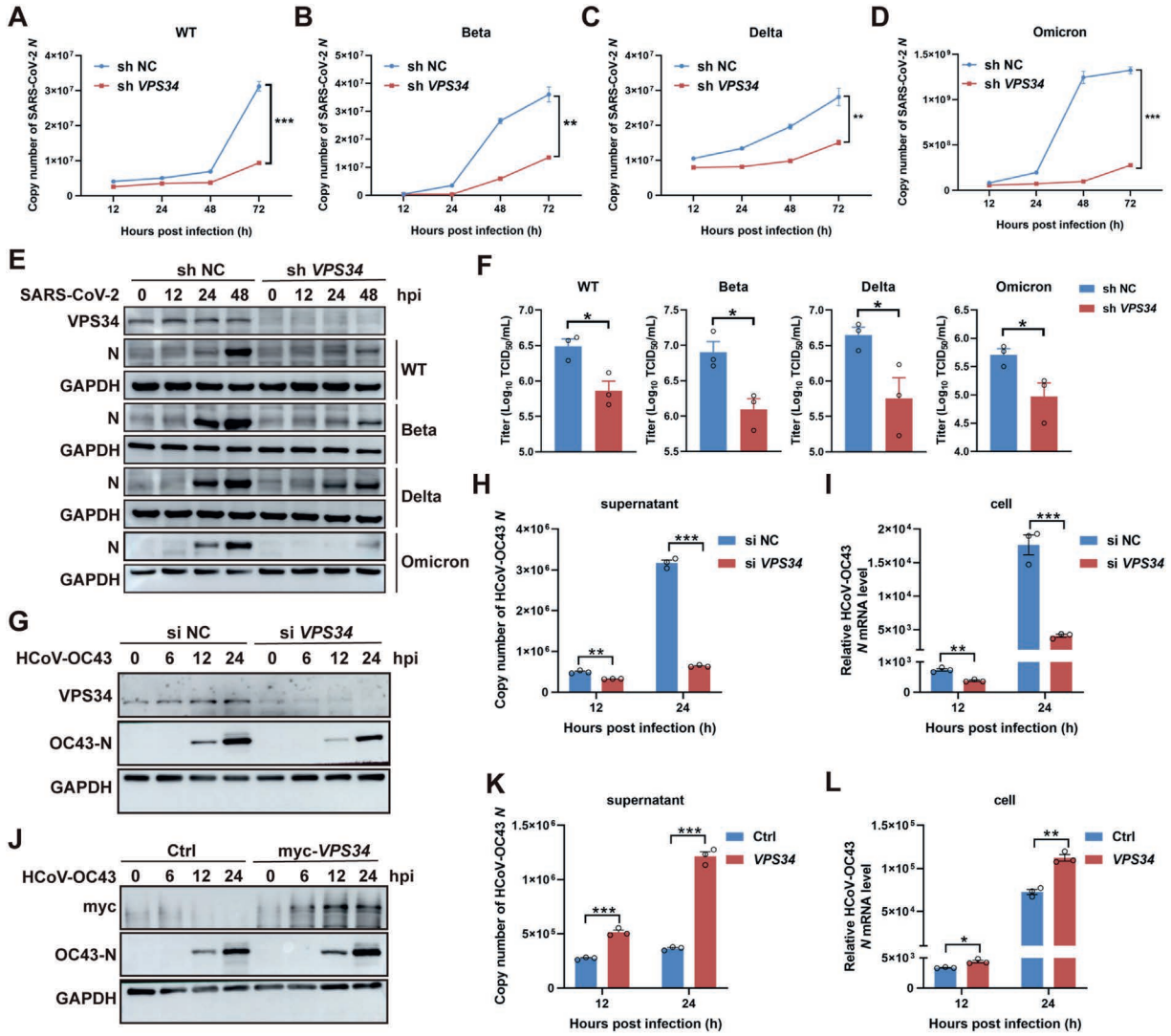


**Figure 1** *VPS34* knockdown inhibits coronavirus infection *in vitro*. (A—E) Multi-step growth curve of SARS-CoV-2. 293-ACE2 cells were transfected with a negative control shRNA or shRNAs targeting human VPS34 for 48 h and then infected with 0.02 MOI SARS-CoV-2 (WT, Beta, Delta, Omicron). Viral replication was monitored by: (A—D) RT-qPCR quantification of *N* gene copies in supernatants at indicated time. (E) Western blot analysis of SARS-CoV-2 N protein levels. (F) SARS-CoV-2 titer was determined by the $TCID_{50}$ assay. (G—L) A549 cells were transfected with si NC, si*VPS34*, control vector (Ctrl), or myc-*VPS34*, and infected with 0.1 MOI HCoV-OC43 at indicated time points. (G, J) The HCoV-OC43 N protein expression was analyzed by Western blot using specific antibodies. (H, K) Viral load in supernatants was assessed through RT-qPCR targeting the HCoV-OC43 *N* gene. (I, L) Intracellular HCoV-OC43 *N* mRNA levels were quantified by RT-qPCR with *GAPDH* normalization. Data are presented as the mean ± SEM ($n = 3$). Statistical significance was analyzed using Student's *t*-test. $^{*}P < 0.05$, $^{**}P < 0.01$, $^{***}P < 0.001$.

CoV-2 strains wild-type (WT; IME-BJ01 strain, GenBank No. MT291831), Beta (CSTR: 16698.06.NPRC2.062100001), Delta (CSTR.16698.06.NPRC6.CCPM-B-V-049-2105-6), Omicron BA.2 (SARS-CoV-2 strain Omicron CoV/human/CHN_CVRI-04/2022), mouse-adapted strain (SARS-CoV-2/C57MA14) were cultured in the biosafety level 3 laboratory as described previously[19,22].

### 2.2. *Inhibitors and antibodies*

VPS34-IN-1 (HY-12795), VPS34-IN-2 (HY-12473), PIK-III (HY-12794), and SAR405 (HY-12481) were purchased from MedChem Express. The antibodies used were as follows: VPS34 (CST, 4263), GAPDH (CST, 5174), SARS-CoV-2 N (SinoBiological, 40143-R001), HCoV-OC43 N (SinoBiological, 40643-T62), HRP-labeled goat anti-rabbit IgG (Beyotime, A0208), HRP-labeled goat anti-mouse IgG (Beyotime, A0216), AF488-labeled goat anti-rabbit IgG (Beyotime, A0423).

### 2.3. *Cell cytotoxicity and antiviral activity assays*

Vero E6 cells (10,000 cells/well) were seeded into 96-well plates and cultured at 37 °C with 5% $CO_2$ for 24 h. The compounds were serially diluted to the indicated concentrations in DMEM, added to the plates, and incubated for 48 h. Cell viability was assessed using CCK-8 assays: 10 μL CCK-8 reagent was added per well,

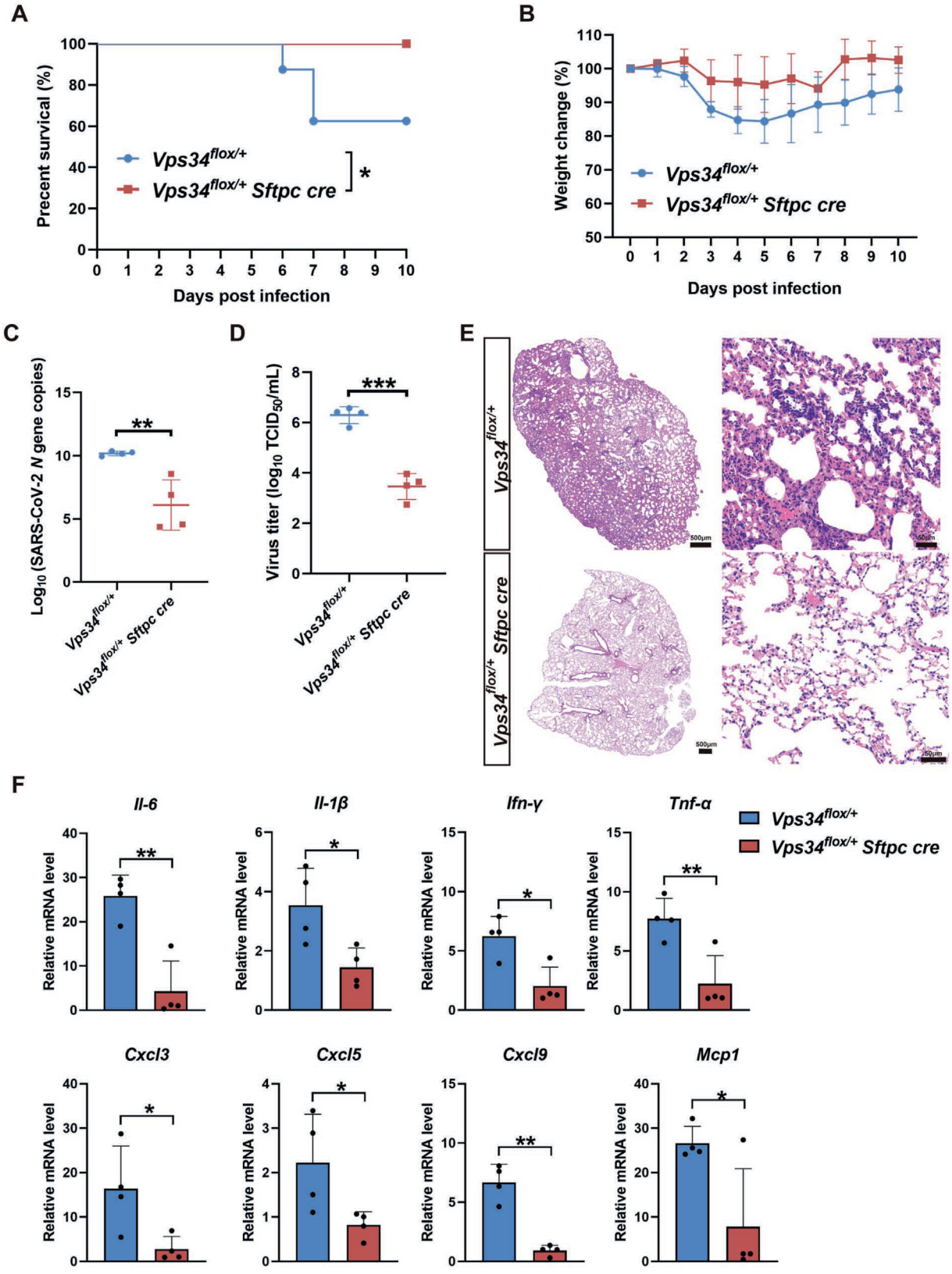


**Figure 2** *VPS34*-deficient mice are resistant to SARS-CoV-2 infection. (A–C) *Vps34*$^{flox/+}$ and *Vps34*$^{flox/+}$ *Sftpc cre* mice were intranasally challenged with 2000 $TCID_{50}$ mouse-adapted SARS-CoV-2. The survival (A) was monitored for 10 days (*Vps34*$^{flox/+}$: $n = 8$, *Vps34*$^{flox/+}$ *Sftpc cre*: $n = 9$). The body weight (B) was monitored for 10 days ($n = 6$). (C–F) Lung tissues were collected at 3 dpi ($n = 4$). (C) SARS-CoV-2 *N* gene in lung tissues was determined by RT-qPCR. (D) Viral titer in lung tissues was determined by $TCID_{50}$ assays. (E) Lung tissues fixed in 4% paraformaldehyde and H&E-stained at 3 dpi. (F) The expression of pro-inflammatory cytokines and chemokines was quantified by RT-qPCR. Data are presented as the mean ± SEM. Statistical analysis was determined by Student's *t*-test and the log-rank test for survival curves. $^{*}P < 0.05$, $^{**}P < 0.01$, $^{***}P < 0.001$.

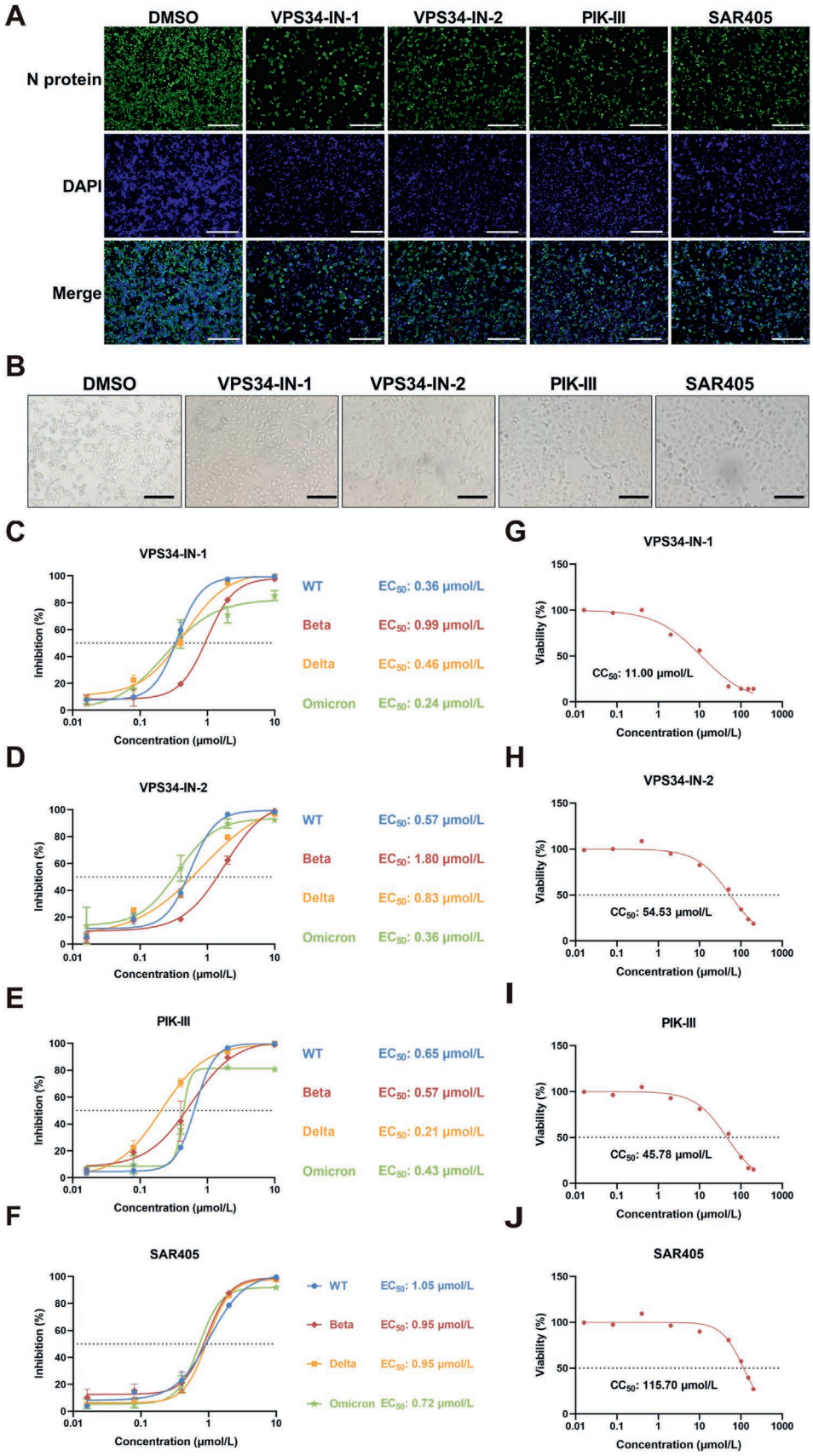


**Figure 3** Inhibition of VPS34 activity decreases coronavirus replication *in vitro*. (A, B) Immuno-fluorescence assay of SARS-CoV-2-infected cells. Vero E6 cells were infected with 0.02 MOI WT SARS-CoV-2 variant and simultaneously treated with VPS34 inhibitors (1 μmol/L). At 48

incubated for 2 h at 37 °C, and the absorbance was measured at 450 nm.

Vero E6 cells (100,000 cells/well) were seeded into 24-well plates and cultured in DMEM supplemented with 2% FBS at 37 °C with 5% $CO_2$ for 24 h. At 2 h post-infection with 0.02 multiplicity of infection (MOI), the culture medium was replaced with compound-containing medium. At 48 hpi, viral RNA was extracted from the supernatant and quantified by amplifying the SARS-CoV-2 *N* gene using qRT-PCR[23,24]. Dose−response curves were analyzed using four-parameter logistic regression to calculate the half-maximal effective concentrations ($EC_{50}$) values relative to that of DMSO controls.

### 2.4. Viral RNA determination

Viral RNA from virus-infected cell supernatants or lysed tissue supernatants was isolated using a FastPure Viral RNA Kit (Vazyme, RC311) according to the manufacturer's instructions. The viral RNA copy number was amplified using the HiScript II U + One Step qRT-PCR Probe Kit (Vazyme, Q223). SARS-CoV-2 RNA copies were determined using a specific probe (5′-FAM-TTGCTGCTGCTTGACAGATT-TAMRA-3′) and primer set (forward 5′-GGGGAACTTCTCCTGCTAGAAT-3′; reverse 5′-CAGACATTTTGCTCTCAAGCT-3′). Following manufacturer protocol, 18 μL One Step PrimeScript RT-PCR kit reaction mixture with 2 μL RNA template was used to perform RT-qPCR assays using the ABI QuantStudio 1.

### 2.5. Immunofluorescent analysis of SARS-CoV-2 infection

Following viral infection, cells were fixed with 4% paraformaldehyde (PFA) for 15 min at room temperature (RT), permeabilized with 0.1% Triton X-100 for 15 min, and blocked with 5% bovine serum albumin (BSA) for 1 h. The cells were then incubated with primary antibody against SARS-CoV-2 N protein overnight at 4 °C, followed by corresponding fluorescent secondary antibody incubation for 1 h at RT. Nuclear counterstaining was performed using DAPI for 5 min before fluorescence microscopy.

### 2.6. Western blotting

Total protein was extracted using a SevenFast Total Protein Extraction Kit (SEVEN BIOTECH, SW-203). Protein concentrations were determined using the BCA kit (Beyotime, P0010). Samples were separated by sodium dodecyl sulfate−polyacrylamide gel electrophoresis and transferred to NC membranes. The membranes were blocked using QuickBlock Blocking Buffer (Beyotime, P0252), incubated with the primary antibodies diluted in QuickBlock Primary Antibody Dilution Buffer (Beyotime, P0256) overnight at 4 °C, and then with HRP-conjugated secondary antibodies for 40 min. Protein bands were visualized using the Pierce ECL Western blot substrate.

### 2.7. Animal experiments

*Vps34*$^{flox/+}$ *Sftpc cre*, *Vps34*$^{flox/+}$, and BALB/c mice were anesthetized and injected intranasally with SARS-CoV-2. Body weights and survival were monitored daily. At 3 days post-infection (dpi), the mice were euthanized and lung tissues were collected for processing. Tissue samples were divided into two groups: one homogenized in PBS for viral load analysis and the other homogenized in TRIzol reagent (Sangon Biotech, B511321) for RNA extraction. The PBS-homogenized tissues were centrifuged at 12,000×*g* for 10 min at 4 °C and the supernatants were analyzed by qRT-PCR to quantify the viral RNA copies. The infectious viral titers were determined using $TCID_{50}$ assays in Vero E6 cells. The total RNA (2 μg) was reverse-transcribed into cDNA using HiScript II Q RT SuperMix (Vazyme, R223), followed by qPCR amplification with SYBR Green Master Mix (Promega, A6001) and primers listed in Supporting Information Table S1. Gene expression was calculated using the $2^{-\Delta\Delta Ct}$ method, normalized to *GAPDH* expression. All experiments were performed in accordance with the Guide for the Care and Use of Laboratory Animals (Approval number: AMMS-11-2023-007).

### 2.8. Histopathological evaluation

The lung tissues were collected and fixed in 4% PFA for 24 h, followed by sequential dehydration in ethanol and paraffin embedding. The sections were stained with hematoxylin and eosin (H&E) following standard histological protocols. Histopathological evaluations were performed using a bright-field microscope.

### 2.9. PK profile and tissue distribution study

For the PK study, the mice received a single intraperitoneal (ip) injection of 10 mg/kg compound. Blood samples were collected 5, 15, 30 min, 1, 2, 4, 6, and 12 h post-dose. Plasma was isolated by centrifuging whole blood at 3000×*g* for 10 min. Plasma compound concentrations were quantified using a validated liquid chromatography−tandem mass spectrometry (LC−MS/MS) method. PK parameters, including $C_{max}$, $T_{max}$, and $t_{1/2,}$ were calculated by noncompartmental analysis using Phoenix WinNonLin v8.0. For tissue distribution analysis, the mice were euthanized 10, 30 min, and 2 h post-ip administration. The liver, lungs, kidneys, heart, and trachea were harvested immediately, rinsed with ice-cold isotonic sodium chloride solution, blotted dry, weighed, and homogenized in 1:10 (*w*/*v*) ice-cold saline. The homogenates were centrifuged at 12,000×*g* for 15 min and the supernatants were analyzed using LC−MS/MS to determine the compound concentrations in the tissue.

### 2.10. Compound synthesis

Step 1: 3-Bromo-5-methylpyridin-2-amine (25.00 g, 133.67 mmol) was placed in a dried eggplant-shaped flask and

hpi, the cells were fixed with 4% paraformaldehyde, permeabilized with 0.1% Triton X-100, and stained using an antiviral nucleocapsid (NP) antibody paired with an Alexa Fluor 488-conjugated secondary antibody (green). The nuclei were counterstained with DAPI (blue). Scale bars: 400 μm. (C−F) Dose-dependent inhibition of SARS-CoV-2 variants by VPS34 inhibitors. Vero E6 cells were infected with 0.02 MOI SARS-CoV-2 variants (WT, Beta, Delta, and Omicron) and simultaneously treated with serially diluted VPS34 inhibitors (VPS34-IN-I, VPS34-IN-2, PIK-III, SAR405). Viral RNA copies in supernatants collected at 48 hpi were quantified *via* RT-qPCR. Inhibition potencies ($EC_{50}$) were calculated based on viral RNA reduction relative to DMSO controls. (G−J) Cytotoxicity evaluation of VPS34 inhibitors. Cell viability was assessed using the CCK-8 assay after 48-h compound exposure. Data represent mean ± SEM from three independent experiments ($n = 3$).

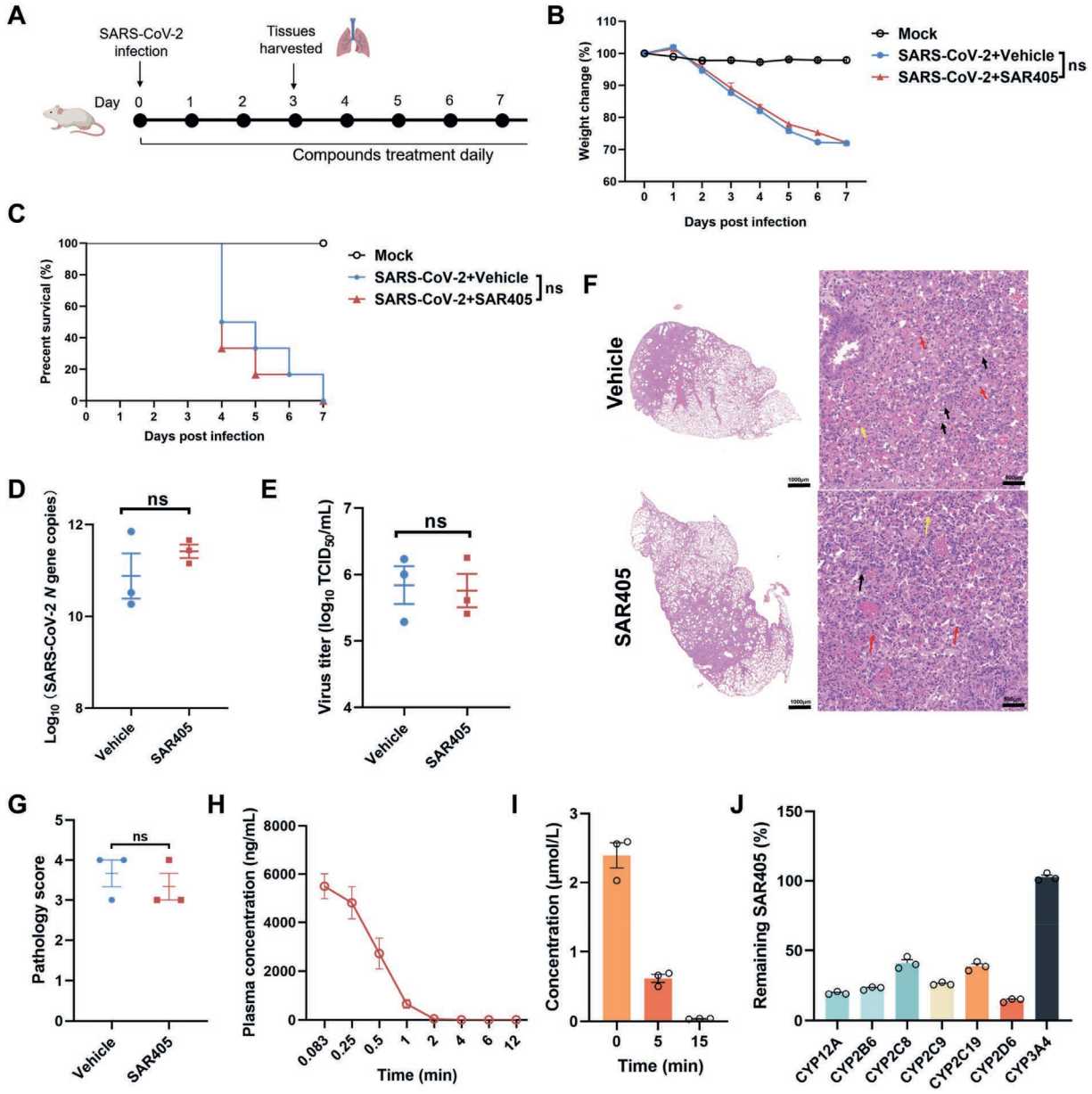


**Figure 4** *In vivo* evaluation of SAR405 against SARS-CoV-2 infection. (A) Diagram of the experimental procedure. BALB/c mice were intranasally infected with $2 \times 10^5$ $TCID_{50}$ SARS-CoV-2. SAR405 (10 mg/kg) or Vehicle was intraperitoneally i.p. administered approximately 2 h pre-infection, followed by once-daily dosing for 7 consecutive days. (B, C) The body weight and survival were monitored for 7 days. (D, E) Lung tissues harvested at 3 dpi were analyzed for SARS-CoV-2 *N* gene copies by RT-qPCR (D) and infectious viral titer by $TCID_{50}$ assay (E) ($n = 3$). (F, G) Histopathological analysis. Lung tissues were fixed in 4% paraformaldehyde and hematoxylin and eosin (H&E)-stained at 3 dpi. (H) The plasma concentration−time profiles of SAR405 in C57BL/6 mice ($n = 3$) after a single intraperitoneal injection (10 mg/kg). (I) Degradation of SAR405 in liver microsomes. (J) Screening of cytochrome P450 enzymes responsible for SAR405 degradation. Data are presented as the mean ± SEM. Statistical analysis was determined by Student's *t*-test and the log-rank test for survival curves. ns, not significant.

dissolved in 300 mL DCM under a nitrogen atmosphere. The solution was cooled to 0 °C and malonyl dichloride (1.10 equiv, 147.00 mmol, 14.30 mL) was added dropwise *via* a pressure-equalizing dropping funnel. The mixture was heated to 25 °C and stirred for 24 h. The precipitated solid was collected by filtration, washed with DCM, and dried to obtain a pale-yellow powder.

Step 2: The product from Step 1 (4.94 g, 19.30 mmol, 1.00 equiv) was charged into a dried eggplant-shaped flask under nitrogen. $POCl_3$ (50 mL) was added and the reaction mixture was heated under reflux at 110 °C for 24 h. After cooling to RT, the mixture was poured into ice-cold water and extracted with DCM ($3 \times 50$ mL). The combined organic layers were dried ($Na_2SO_4$) to yield the intermediate for further use.

Step 3: The intermediate obtained from Step 2 was transferred to an eggplant-shaped flask, followed by the addition of anhydrous ethanol (50 mL) and *R*-methylmorpholine (5 g, 49.43 mmol). The mixture was heated under reflux at 80 °C for 24 h. Upon cooling to RT, a white precipitate formed, which was filtered, washed with ethanol, and dried.

Step 4: The white solid from Step 3 (338.00 mg, 1.00 mmol, 1.00 equiv) was combined with 1-amino-3,3-dimethylbutan-2-one (1.20 equiv), Pd(dppf)$Cl_2$ (45.00 mg), and *t*-BuONa (2.00 equiv, 2.00 mmol, 193.00 mg) in THF (25 mL). The mixture was then refluxed for 24 h. After removing THF by rotary evaporation, the residue was extracted with 1:1 (*v*/*v*) $H_2O$/DCM. The organic layer was dried ($Na_2SO_4$) and purified by column chromatography (silica gel, hexane/EtOAc) to obtain the final product.

### 2.11. Molecular docking

The experimental procedure commenced with retrieval of the VPS34 crystal structure from the PDB database. The protein structure was subsequently processed using PyMOL to remove the crystallographic water molecules and original ligands. The prepared protein structure and small-molecule ligands were imported into AutoDock Tools for hydrogenation. Molecular docking was performed using AutoDock Vina to identify optimal conformations and calculate corresponding binding affinities. The docking results were visualized using PyMOL for 3D representations and Discovery Studio for 2D interaction diagrams.

### 2.12. Surface plasmon resonance (SPR) assay

The VPS34 protein (Sino Biological, P26-102G) was immobilized on the sensor chip surface. Each test compound was serially diluted in a 96-well plate and injected over the target protein-coupled surface in order of increasing concentration. The injection parameters were: flow rate 30 μL/min, contact time 150 s. After each concentration cycle, the chip surface was regenerated for 5 min using 10 mmol/L glycine-HCl (pH 2.0). This process was repeated until all compound concentrations had been analyzed. $K_D$ values were obtained by globally fitting the data to a 1:1 Langmuir binding model using Biacore Insight Evaluation Software (Cytiva, Marlborough, MA, USA).

### 2.13. Statistical analysis

Data were analyzed with GraphPad Prism 8.0 software. The significance of each difference was assessed using a *t*-test or ANOVA, accompanied by a two-tailed *t*-test. Statistical significance was set at $P < 0.05$.

## 3. Result

### 3.1. VPS34 knockdown suppresses coronavirus infection in vitro

To determine the critical role of VPS34 in coronavirus infection, we employed *VPS34* knockdown technology by designing three *VPS34*-targeting short hairpin RNAs (shRNAs) in 293ACE2 cells. The efficiency of *VPS34* knockdown in 293-ACE2 cells was approximately 80% (Supporting Information Fig. S1A). Then, 293-ACE2 shNC and 293-ACE2 sh*VPS34* cells were infected with 0.1 MOI SARS-CoV-2 and harvested at 12, 24, 48, and 72 h to measure viral replication. *VPS34* knockdown significantly reduced WT SARS-CoV-2 RNA levels (Fig. 1A), N protein expression (Fig. 1E), and viral titers (Fig. 1F). Three SARS-CoV-2 variants, Beta, Delta, and Omicron, were used to infect shNC and sh*VPS34* cells. Similarly, *VPS34* depletion markedly inhibited the replication of these SARS-CoV-2 variants (Fig. 1B−F). As coronaviruses rely on autophagy machinery to generate DMVs essential for viral replication, it is reasonable to speculate that VPS34 has broad-spectrum anti-coronavirus activity[25,26]. To validate this hypothesis, we evaluated the impact of VPS34 inhibition on the replication cycle of another *β*-coronavirus. The data show that HCoV-OC43 production was significantly reduced in the A549 si*VPS34* cells (Fig. 1G−I). Meanwhile, we overexpressed *VPS34* in A549 cells, and the results showed that *VPS34* overexpression promoted the replication of HCoV-OC43 (Fig. 1J−L). Taken together, these results provide evidence that VPS34 knockdown inhibits coronavirus infection *in vitro*.

### 3.2. VPS34-deficient mice are resistant to SARS-CoV-2 infection

To further evaluate the important role of VPS34 in pneumonia caused by SARS-CoV-2 infection, we infected *Vps34*-deficient mice with mouse-adapted SARS-CoV-2. This model results in severe lung disease resembling lung injury in humans and is widely used for evaluating SARS-CoV-2 therapeutics and vaccine candidates[27,28]. A previous study found that conditional *Vps34* knockout caused muscular dystrophy in mice, which began to exhibit progressive disease onset and mortality starting at 42 days postnatally[29]. We used the Cre−loxP system to generate tissue-specific *Vps34* knockdown mice (*Vps34*$^{flox/+}$ *Sftpc Cre*). The VPS34 protein levels in the lungs of *Vps34*$^{flox/+}$ *Sftpc cre* mice decreased, as verified by Western blotting (Fig. S1B). *Vps34*$^{flox/+}$ and *Vps34*$^{flox/+}$ *Sftpc cre* mice were infected with SARS-CoV-2 and their survival and body weight changes were monitored daily for 10 days. Among the *Vps34*$^{flox/+}$ mice, 3/8 (37.5%) succumbed by day 7 post-intervention, whereas all *Vps34*$^{flox/+}$ *Sftpc cre* mice survived (Fig. 2A). Notably, *Vps34*$^{flox/+}$ *Sftpc cre* mice showed attenuated body weight loss (Fig. 2B). The SARS-CoV-2 titers in lung tissues at 3 dpi were evaluated and compared, suggesting that the *N* gene copy number and viral titers were significantly lower in *Vps34*$^{flox/+}$ *Sftpc cre* mice than in *Vps34*$^{flox/+}$ mice (Fig. 2C and D). Histopathological analysis of the lungs revealed distinct phenotypes between the genotypes. *Vps34*$^{flox/+}$ mice exhibited disorganized alveolar architecture with structural collapse, accompanied by sparse inflammatory cell infiltration and focal necrotic lesions. In contrast, *Vps34*$^{flox/+}$ *Sftpc cre* mice showed preserved alveolar integrity with well-defined septal boundaries and no significant inflammatory infiltrates or cellular necrosis, consistent with attenuated pulmonary injury (Fig. 2E, Supporting Information Fig. S2). Meanwhile, *Vps34*$^{flox/+}$ *Sftpc cre* mice showed a marked reduction in the expression of genes encoding pro-inflammatory cytokines and chemokines (Fig. 2F). Taken together, these findings demonstrate that VPS34 is an essential host factor that facilitates SARS-CoV-2 infection and pathogenesis.

### 3.3. The high antiviral activities of VPS34 inhibitors in SARS-CoV-2-infected cells

Using genetic editing technology, we confirmed that VPS34 is a critical host factor for coronavirus replication. Based on this, we further explored the discovery of highly effective antiviral inhibitors targeting VPS34 as potential lead compounds. The antiviral efficacy of VPS34 inhibitors against SARS-CoV-2 was evaluated by immunofluorescence microscopy and quantitative analysis of viral nucleoprotein expression. The data in Fig. 3A shows that all VPS34 inhibitors, including VPS34-IN-1, VPS34-IN-2, PIK-III, and SAR405, exhibited similar inhibition of SARS-CoV-2 infection. Notably, all four VPS34 inhibitors protected cells from SARS-CoV-2-induced CPE, highlighting the critical role of VPS34 in SARS-CoV-2 infection (Fig. 3B). Antiviral activity was quantified by measuring viral RNA copies using

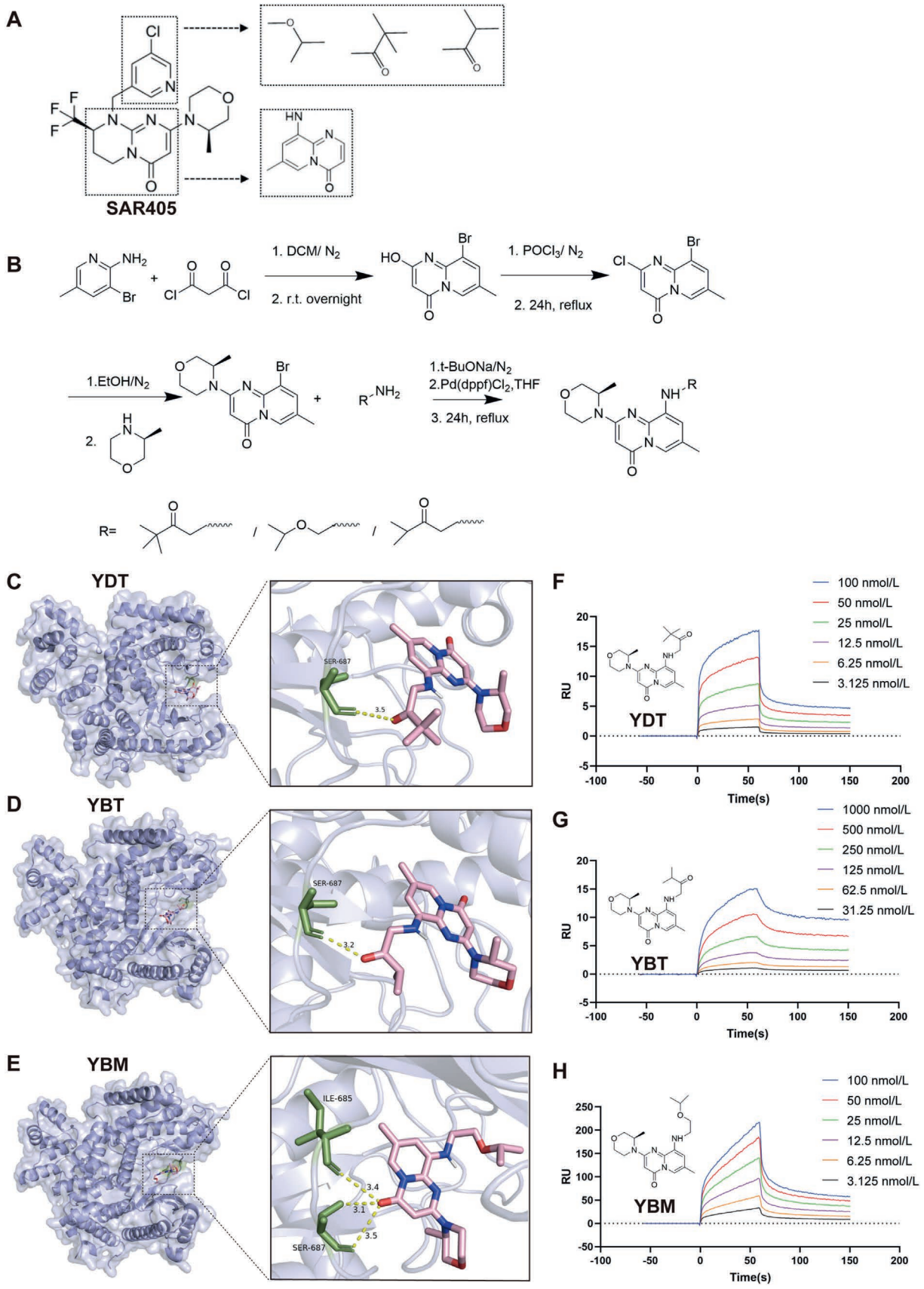
A
SAR405
B
1. DCM/ N2
2. r.t. overnight
1. POCl3/ N2
2. 24h, reflux
1.EtOH/N2
2.
1.t-BuONa/N2
2.Pd(dppf)Cl2,THF
3. 24h, reflux
R=
C
YDT
SER-687
3.5
D
YBT
SER-687
3.2
E
YBM
ILE-685
3.4
3.1
SER-687
3.5
F
100 nmol/L
50 nmol/L
25 nmol/L
12.5 nmol/L
6.25 nmol/L
3.125 nmol/L
YDT
RU
Time(s)
G
1000 nmol/L
500 nmol/L
250 nmol/L
125 nmol/L
62.5 nmol/L
31.25 nmol/L
YBT
RU
Time(s)
H
100 nmol/L
50 nmol/L
25 nmol/L
12.5 nmol/L
6.25 nmol/L
3.125 nmol/L
YBM
RU
Time(s)

RT-qPCR, with $EC_{50}$ derived from the dose−response curves. Cell viability assays were performed to determine the half-maximal cytotoxic concentrations ($CC_{50}$) of each compound. The selectivity index (SI) was calculated as $CC_{50}/EC_{50}$. As shown in Fig. 3C−F, pharmacological profiling of VPS34 inhibitors against SARS-CoV-2 variants demonstrated that the $EC_{50}$ of VPS34-IN-1 were 0.36, 0.99, 0.46, and 0.24 μmol/L against WT, Beta, Delta, and Omicron variants, respectively; VPS34-IN-2 were 0.57, 1.80, 0.83, and 0.36 μmol/L against WT, Beta, Delta, and Omicron, respectively; PIK-III were 0.65, 0.57, 0.21, and 0.43 μmol/L against WT, Beta, Delta, and Omicron variants, respectively; and SAR405 were 1.05, 0.95, 0.95, and 0.72 μmol/L against WT, Beta, Delta, and Omicron variants, respectively. Cytotoxicity assessments revealed that the $CC_{50}$ of VPS34-IN-1, VPS34-IN-2, PIK-III, and SAR405 were 11.00, 54.53, 45.78, and 115.70 μmol/L, respectively (Fig. 3G−J). The calculated SI identified SAR405 as the most potent compound, with the SI range being 110.19 (WT) to 160.69 (Omicron).

We further evaluated the anti-HCoV-OC43 activity of VPS34 inhibitors, which showed dose-dependent viral replication suppression. The measured $EC_{50}$ of VPS34-IN-1, VPS34-IN-2, PIK-III, and SAR405 were 0.51, 0.75, 0.68, and 0.34 μmol/L, respectively (Supporting Information Fig. S3A−S3D). The cells were partially protected from the HCoV-OC43-induced CPE by these inhibitors (Fig. S3E). SAR405 exhibited the most potent antiviral activity among the tested compounds, which correlated with its superior enzymatic inhibitory potency against VPS34 (VPS34 IN-I, 25 nmol/L; VPS34 IN-2, 2 nmol/L; PIK-III, 18 nmol/L; SAR405, 1.2 nmol/L)[30-33]. Based on this pharmacological profile, SAR405 was selected for subsequent *in vivo* antiviral studies and as a lead compound for structural optimization.

### 3.4. *In vivo antiviral efficacy and PK profiling of SAR405*

Next, we tested whether SAR405 could inhibit SARS-CoV-2 replication *in vivo* using BALB/c mice infected with mouse-adapted SARS-CoV-2 and treated with SAR405 or Vehicle (Fig. 4A). Consistent with the *in vivo* protocol established by Noman MZ[21], 10 mg/kg SAR405 was administered to mice *via* oral gavage, which significantly suppressed tumor growth. Using this validated dosage regimen, we conducted a parallel *in vivo* antiviral efficacy study. The data in Fig. 4B and C showed that all SARS-CoV-2-infected mice exhibited similar disease progression without statistically significant differences. Notably, SAR405 treatment did not reduce SARS-CoV-2 replication in the lungs of infected mice at 3 dpi (Fig. 4D and E). Furthermore, we collected the lungs from infected mice to evaluate the histological changes. The lung tissue injury patterns observed in both SAR405-and Vehicle-treated groups exhibited comparable severity (Fig. 4F and G). Histopathological analysis revealed moderate structural abnormalities characterized by indistinct alveolar architecture with localized areas of marked collapse and alveolar septal thickening. A notable increase in epithelial cellularity and substantial parenchymal consolidation were evident throughout the tissue sections. Extensive neutrophil infiltration within the consolidated parenchyma was consistently observed (indicated by red arrows). Scattered instances of cellular necrosis and karyorrhexis (nuclear fragmentation) are occasionally observed (black arrows). Tissue sections demonstrated significantly elevated red blood cell extravasation (highlighted by yellow arrows).

Although SAR405 demonstrated potent *in vitro* antiviral activity against SARS-CoV-2, it did not demonstrate comparable antiviral efficacy *in vivo*. This discrepancy may arise from suboptimal PK properties, including inadequate systemic absorption and insufficient tissue distribution to viral replication sites, most critically to the lungs, the principal site of SARS-CoV-2 replication and pathogenesis. To investigate this, we characterized the PK profile of SAR405 after a single IP dose and assessed its tissue-specific accumulation in the heart, liver, lungs, kidneys, and trachea. The plasma concentration−time profiles after IP administration of 10 mg/kg SAR405 are presented in Fig. 4H, and the main pharmacokinetic parameters are listed in Supporting Information Table S2. After ip administration of 10 mg/kg SAR405, PK analysis revealed rapid absorption kinetics ($C_{max}$ = 5821.66 ± 723.13 ng/mL; $T_{max}$ = 0.14 ± 0.1 h) coupled with accelerated systemic clearance (CL = 3250.94 ± 1081.29 mL/h/kg; $t_{1/2}$ = 1.83 ± 1.97 h). The limited systemic exposure ($AUC_{last}$ = 3279.65 ± 930.9 h ng/mL) indicates pronounced first-pass metabolism. Following IP administration of SAR405, $C_{max}$ were achieved within 10 min across cardiorespiratory and renal systems (Supporting Information Table S3). To further elucidate the specific reasons for the poor systemic exposure of SAR405, we simulated the *in vivo* metabolic environment using liver microsomes. The results demonstrated that SAR405 was extensively degraded to minimal levels within 15 min in the liver microsomes (Fig. 4I). Concurrently, we screened the major cytochrome P450 (CYP450) enzymes involved in SAR405 degradation. The screening results revealed that the degradation of SAR405 was almost completely attenuated upon addition of 6$\beta$-hydroxytestosterone, a specific inhibitor of CYP3A4 (Fig. 4J). These findings collectively indicate that SAR405 is rapidly degraded by CYP3A4 after absorption and entry into the systemic circulation. Paradoxically, therapeutically relevant concentrations fail to accumulate in SARS-CoV-2 target organs. The collective PK−pharmacodynamic (PK/PD) disconnect observed in SAR405 highlights a critical therapeutic barrier: rapid systemic clearance and subtherapeutic target site exposure, culminating in insufficient antiviral coverage.

### 3.5. *Design and synthesis of derivatives based on the lead compound SAR405*

To enhance the PK properties and preclinical development of SAR405, we systematically modified the lead compound structure. In rational drug design, the introducing isopropoxy ($-OCH(CH_3)_2$), isobutyryl ($-COCH(CH_3)_2$), and pivaloyl ($-COC(CH_3)_3$) groups based on chemical group properties including electronic effects, steric hindrance, and metabolic stability significantly optimized the PK properties. To overcome the limitations of SAR405 absorption and metabolism *in vivo*, we replaced specific moieties in the scaffold and incorporated aliphatic chains to generate new compounds (Fig. 5A and B). Using the VPS34 crystal structure (PDB: 4OYS), we proposed the

**Figure 5** The discovery of potent and selective VPS34 inhibitors. (A) Schematic representation of group substitutions in SAR405. (B) Synthetic route for SAR405 derivatives. (C−E) Structural formulas of SAR405 derivatives and 3D views of their molecular docking with VPS34. (F−H) Interactions between SAR405 derivatives and VPS34 were analyzed using SPR.

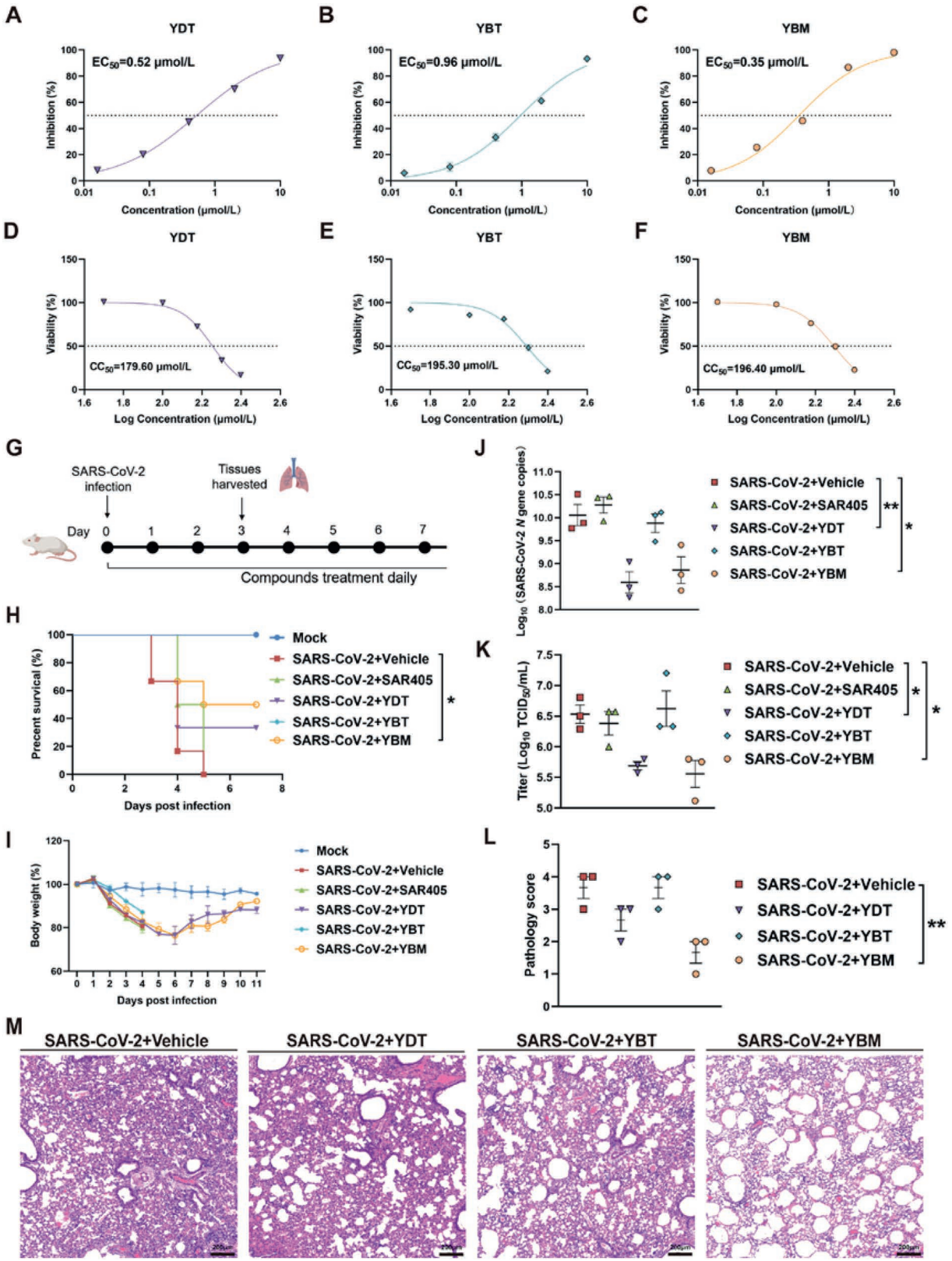


**Figure 6** Therapeutic evaluation of SAR405 derivatives in SARS-CoV-2-infected mice. (A−C) Dose-dependent inhibition of SARS-CoV-2 by SAR405 derivatives. Vero E6 cells were infected with 0.02 MOI SARS-CoV-2 variants (WT) and simultaneously treated with serially diluted compounds. Viral RNA copies in supernatants collected at 48 hpi were quantified *via* RT-qPCR. Inhibition potencies ($EC_{50}$) were calculated based on viral RNA reduction relative to DMSO controls. (D−F) Cytotoxicity evaluation of SAR405 derivatives. Cell viability was assessed using the CCK-8 assay after 48-h compound exposure. (G) Diagram of the experimental procedure. BALB/c mice were intranasally infected with $2 \times 10^5$

binding modes between VPS34 and the three compounds. In YDT's binding to the VPS34 protein (Fig. 5C, Supporting Information Fig. S4A), the aromatic ring structure of the molecule forms a key Pi−Sigma interaction with the aromatic side chain of the Phe612 residue. This is crucial for maintaining the planar stacking binding mode of the molecule, thereby enhancing binding specificity and affinity. Multiple alkyl substituents engage in Pi−Alkyl interactions with the aliphatic side chains of residues such as Ile634 and Ile760. These hydrophobic interactions effectively fill the hydrophobic pocket of the protein, improving binding stability. Additionally, the alkyl chains in the molecule further reinforce the hydrophobic binding region through Alkyl interactions with residues such as Leu750 and Ile685. Meanwhile, van der Waals interactions between the molecular surface and residues like Met682 and Asp761 assist in the spatial accommodation of the molecule within the active pocket, providing steric support for the overall binding.

In YBT's binding to the VPS34 protein (Fig. 5D, Fig. S4B), the aromatic system forms a Pi−Sigma interaction with the Phe612 residue, serving as a critical force for anchoring the molecule in the protein's active center and laying the foundation for subsequent multidimensional binding. The hydrophobic side chains of residues such as Ile634 and Ile760 align with the Pi−Alkyl interaction sites of the compound, strengthening hydrophobic binding through Pi−Alkyl interactions. Alkyl structures of residues like Pro618 and Leu750 form Alkyl interactions with the alkyl portions of YBT, further consolidating the strength of hydrophobic binding. van der Waals interactions between residues such as Ser614 and Asp761 and the YBT molecule contribute to the spatial adaptability of the molecule within the protein's active pocket, ensuring a stable binding conformation.

In YBM's binding to the VPS34 protein (Fig. 5E, Fig. S4C), the Pi−Sigma interaction between the aromatic group of this compound and the Phe612 residue serves as the core aromatic driving force for molecular binding to the protein, playing a significant role in the initiation and orientation of binding. The hydrophobic regions of residues such as Ile634 and Ile760 tightly engage with the Pi−Alkyl interaction sites of YBM through Pi−Alkyl interactions, enhancing the contribution of hydrophobic effects to binding. Alkyl portions of residues like Pro618 and Leu750 form Alkyl interactions with the alkyl chains of YBM, further optimizing hydrophobic binding. Notably, YBM contains groups capable of forming a Conventional Hydrogen Bond with the Ser687 residue. This strong polar interaction significantly enhances the affinity and specificity of the molecule's binding to the protein. Simultaneously, van der Waals interactions between residues such as Gln683 and Met682 and the YBM molecule facilitate stable binding within the active pocket from a spatial matching perspective. Multiple forces synergistically ensure the effective binding of YBM to the VPS34 protein.

To quantitatively evaluate the interaction between these compounds and VPS34, we performed surface plasmon resonance (SPR) assays. As shown in Fig. 5F−H, all three compounds exhibited concentration-dependent binding to VPS34, with the following equilibrium dissociation constants ($K_D$): YDT $K_D$: $5.27 \times 10^{-8}$ mol/L, YBT $K_D$: $7.36 \times 10^{-7}$ mol/L, YBM $K_D$: $2.19 \times 10^{-8}$ mol/L. The $K_D$ indicates that YBM has the highest binding affinity for VPS34. In summary, the compounds (YDT, YBT, YBM) achieve effective binding with the VPS34 protein through multiple intermolecular interactions.

### 3.6. *Inhibitor of VPS34, YBM, blocked SARS-CoV-2 replication*

The antiviral potential of SAR405 derivatives (YDT, YBT, YBM) was systematically evaluated in Vero E6 cells through assessment of viral inhibition and cellular safety profiles. Quantitative analysis of SARS-CoV-2 replication inhibition (Fig. 6A−C) revealed concentration-dependent effects, with YBM demonstrating the most potent activity ($EC_{50}$ = 0.35 μmol/L), followed by YDT ($EC_{50}$ = 0.52 μmol/L) and YBT ($EC_{50}$ = 0.96 μmol/L). Cytotoxicity assessment *via* CCK-8 assays (Fig. 6D−F) showed significant improvement over SAR405, with $CC_{50}$ values of 196.40 (YBM), 195.30 (YBT), and 179.60 μmol/L (YDT), representing 1.6-fold increases in safety margins compared to SAR405. These demonstrate successful retention of antiviral activity alongside reduced cytotoxicity through structural optimization.

To investigate the PK profile and anti-SARS-CoV-2 efficacy of the newly synthesized VPS34-targeting compounds (YDT, YBT, and YBM), we first compared their systemic exposure profiles with those of the parent compound, SAR405, in mice. As shown in Supporting Information Fig. S5A, YBM reached a maximum plasma concentration of 14,327.90 ± 1322.77 ng/mL at 5 min post-ip injection, approximately 2.6-fold higher than that of SAR405. This was accompanied by a significantly reduced clearance rate (Supporting Information Table S4), which corresponded to a 5.3-fold improvement in systemic retention. Tissue distribution analysis revealed superior lung accumulation of YBM 10, 30, and 120 min post-ip injection, with the concentrations consistently exceeding those of SAR405, YDT, and YBT (Fig. S5B, Supporting Information Table S5).

Antiviral evaluation of the infected mice (Fig. 6G) showed complete mortality in the Vehicle-, SAR405-, and YBT-treated groups at 5 dpi. In contrast, the YDT- and YBM-treated groups showed 33% and 50% survival rates, respectively (Fig. 6H). Surviving mice in the YDT/YBM group showed transient weight loss (75% initial weight at 6 dpi), followed by recovery starting at 7 dpi (Fig. 6I). At 3 dpi, YDT and YBM treatments significantly reduced lung SARS-CoV-2 N gene copies (Fig. 6J) and viral loads (Fig. 6K) compared to the Vehicle treatment. Histopathological analysis of H&E-stained lung sections demonstrated that YBM-treated mice exhibited attenuated inflammatory infiltration and an absence of overt cellular necrosis despite partial disorganization of the alveolar architecture with regional collapse, in contrast to vehicle-treated controls, which displayed extensive inflammatory pathology (Fig. 6L−M). Owing to SARS-CoV-2-induced cytokine/chemokine dysregulation, we measured pulmonary pro-inflammatory cytokine (*Il-6*, *Il-1β*, *Ifn-γ*, *Tnf-α*) and chemokine (*Cxcl3*, *Cxcl5*, *Cxcl9*, *Mcp1*) levels. YDT and YBM suppressed pro-inflammatory mediator expression and mitigated the cytokine

$TCID_{50}$ SARS-CoV-2. SAR405, YDT, YBT, YBM, and Vehicle were intraperitoneally administered approximately 2 h pre-infection, followed by once daily for 7 consecutive days. (H, I) The survival and body weight were monitored for 7 days. (J, K) Lung tissues harvested at 3 dpi were analyzed for SARS-CoV-2 *N* gene copies by RT-qPCR (J) and infectious viral titer by $TCID_{50}$ assay (K) ($n$ = 3). (L−M) Histopathological analysis. Lung tissues were fixed in 4% paraformaldehyde and H&E-stained at 3 dpi. Data represent mean ± SEM. Statistical significance was determined by two-way ANOVA and log-rank test for survival curves. *$P < 0.05$, **$P < 0.01$, ***$P < 0.001$.

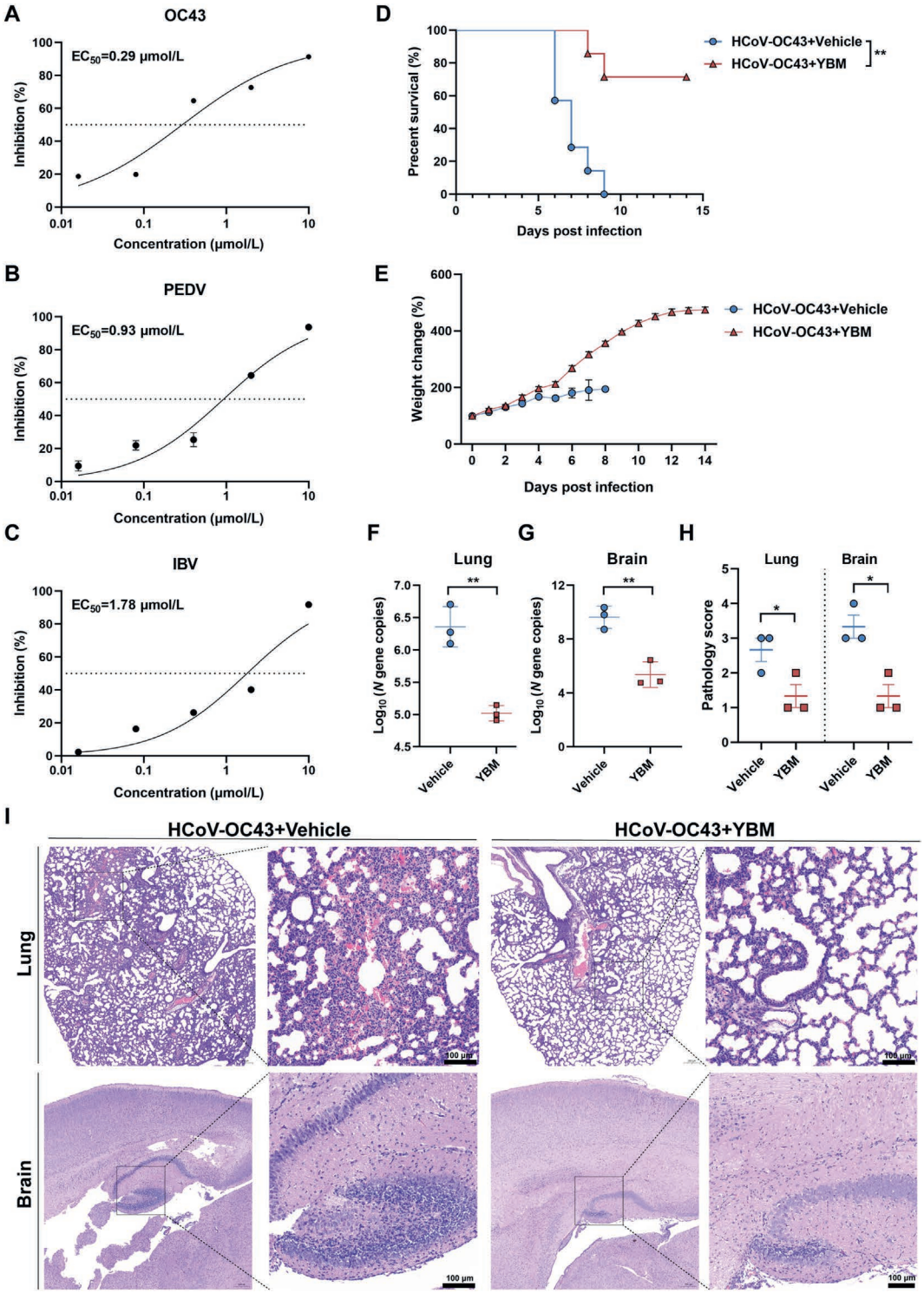


**Figure 7** YBM has broad-spectrum activity against coronaviruses. (A) Dose-dependent HCoV-OC43 inhibition by YBM. BEAS-2B cells were infected with 0.1 MOI HCoV-OC43 and simultaneously treated with serially diluted YBM. (B, C) Vero E6 cells were infected with 0.1 MOI PEDV or IBV and simultaneously treated with serially diluted YBM. Viral RNA copies in supernatants collected at 72 hpi were quantified *via* RT-qPCR. The $EC_{50}$ were calculated based on viral RNA reduction relative to DMSO controls. (D−I) *In vivo* efficacy of YBM against HCoV-OC43 infection in Newborn mice. 3-day-old mice were intranasally infected with $10^2$ $TCID_{50}$ HCoV-OC43. YBM (10 mg/kg) or Vehicle was intraperitoneally IP, followed by once-daily dosing for 14 consecutive days. (D, E) The survival and body weight were monitored for 14 days ($n = 7$). (F, G) Lung and brain tissues harvested at 5 dpi were analyzed for HCoV-OC43 *N* gene copies by RT-qPCR. (H, I) Histopathological analysis. Lung tissues and brain tissues were fixed in 4% paraformaldehyde and H&E-stained at 5 dpi. Data represent mean ± SEM from three independent experiments. Statistical analysis was determined by Student's *t*-test and the log-rank test for survival curves. $^*P < 0.05$, $^{**}P < 0.01$.

storm severity (Supporting Information Fig. S6). These results demonstrate that structural optimization of SAR405, particularly YBM, enhances both its PK properties and antiviral efficacy by improving systemic exposure, lung targeting, and dual suppression of viral replication and inflammation. Thus, YBM can serve as a potent VPS34-targeting drug candidate for further optimization and drug development studies.

### *3.7. YBM has broad-spectrum activity against coronaviruses*

To further investigate the broad-spectrum anti-coronavirus potential of YBM, we evaluated its inhibitory effects against representative strains from three coronavirus genera: $\alpha$-coronavirus (Porcine Epidemic Diarrhea Virus, PEDV), $\beta$-coronavirus (HCoV-OC43), and $\gamma$-coronavirus (Infectious Bronchitis Virus, IBV) in cellular assays. As shown in Fig. 7A−C, YBM exhibited dose-dependent inhibition of viral replication across all tested strains, with $EC_{50}$ comparable to those observed for SARS-CoV-2. The *in vivo* efficacy of YBM against $\beta$-coronavirus infection was evaluated using HCoV-OC43. Mortality analysis revealed striking differences between the YBM-treated group and the Vehicle group (Fig. 7D). Continuous body weight monitoring over 14 days demonstrated that the YBM-treated group maintained steady weight gain (Fig. 7E). The viral load in the lung and brain tissues of mice on 5 dpi was detected. The results showed a significant reduction in the HCoV-OC43 *N* gene in the lung and brain tissues in the YBM-treated group, and the viral load was also significantly lower than Vehicle group (Fig. 7F and G). H&E staining results of lung tissue revealed extensive atrophy and disorganization of alveolar structures with significant thickening of alveolar walls, whereas the YBM-treated group exhibited essentially normal lung tissue architecture with intact alveoli (Fig. 7H and I). HE staining of brain tissue showed severe structural abnormalities in the Vehicle group, characterized by extensive neuronal degeneration, including shrunken and deeply stained cell. In contrast, the YBM-treated group displayed only mild structural abnormalities with abundant neurons in the hippocampal region and minimal neuronal degeneration (Fig. 7H and I). Together, these results demonstrate that YBM has broad-spectrum anti-coronavirus activity.

### *3.8. YBM inhibits autophagy and has low toxicity in vivo*

Given the important role of VPS34 in autophagy, we investigated the effects of YBM on this pathway. In A549 cells subjected to EBSS-induced starvation, a marked increase in LC3-II conversion was observed, indicative of autophagy activation. Notably, YBM treatment dose-dependently suppressed this LC3-II conversion (Supporting Information Fig. S7A). For p62, a selective autophagy substrate, revealed progressive accumulation upon YBM treatment, further confirming autophagy flux blockade (Fig. S7B). These data establish YBM as a potent autophagy inhibitor targeting the VPS34 pathway. To address potential safety concerns from chronic autophagy suppression, longitudinal toxicity studies were conducted in mice. Body weight monitoring demonstrated parallel growth trajectories across all treatment groups and the control group throughout the observation period (Fig. 8A). Serum biochemical analyses further confirmed the absence of statistically significant alterations in hepatic (ALT, AST, ALP, TBIL-Z, DBIL-Z, TP, GGT, TBA, ALB) and renal (UA, BUN, CREA, MALB, NAG) function biomarkers relative to controls (Fig. 8B−O). Histopathological assessment of heart, liver, spleen, lung, and kidney tissues staining revealed no detectable abnormalities (Fig. 8P). Collectively, these findings demonstrate excellent tolerability of YBM at both therapeutic and supra-therapeutic doses.

## 4. Discussion

The ongoing emergence of novel coronaviruses, particularly SARS-CoV-2, has posed unprecedented challenges to global public health. Recently, there has been an alarming surge in coronavirus outbreaks including SARS-CoV in 2003, MERS-CoV in 2012, and the ongoing SARS-CoV-2 pandemic initiated in 2019[34-37]. Although vaccination campaigns have moderately succeeded in reducing infection rates and transmission dynamics, persistent threats necessitate the urgent development of broad-spectrum anti-CoV therapeutics. This is further amplified by the evolutionary race between host immunity and viral immune evasion mechanisms, as exemplified by the rapid emergence of SARS-CoV-2 variants with enhanced transmissibility and antibody-escape capabilities. While protease inhibitors such as molnupiravir and Paxlovid™ have received clinical approval, therapeutic agents targeting host factors essential for coronavirus replication remain critically underexplored[7,38]. In this study, we demonstrated that both *in vitro* and *in vivo VPS34* knockdown significantly attenuated coronavirus replication, validating VPS34 as a promising host-directed therapeutic target against coronavirus infection. Moreover, building upon the VPS34 inhibitor SAR405 as a lead compound, we rationally designed YBM, a novel VPS34-targeting inhibitor that demonstrated excellent *in vivo* antiviral efficacy while maintaining improved PK properties.

VPS34, the sole PI3K in mammals, plays essential roles in autophagy, endosomal trafficking, and other cellular processes. VPS34-mediated phosphatidylinositol 3-phosphate (PI3P) generation enables the membrane recruitment of effector proteins for endosomal fusion, assembly of endosomal sorting complexes required for transport (ESCRT) during multivesicular body formation, and retromer complex stabilization for endosome-to-Golgi retrograde transport[39,40]. For RNA viruses, such as Ebola virus (EBOV) and tomato bushy stunt virus (TBSV), VPS34 is recruited to viral replication compartments, elevating PI3P levels that facilitate Rab5-positive early endosome recruitment, thereby providing phosphatidylethanolamine-enriched membranes for replication complex assembly[41,42]. Mechanistically, both HCV and SARS-CoV-2 exploit VPS34-catalyzed PI3P production and its effector DFCP1 to scaffold DMV formation, which serves as a critical platform for viral RNA replication[18]. Although previous studies have identified the antiviral potential of VPS34 through high-throughput screening, these findings were predominantly limited to cell culture systems, leaving the in *vivo* therapeutic efficacy uncharacterized[43-45]. Using genetic knockdown approaches, we demonstrated that *VPS34* suppression significantly inhibits coronavirus replication both *in vitro* and *in vivo*. Pharmacological validation using VPS34 inhibitors (VPS34-IN-1, VPS34-IN-2, PIK-III, and SAR405) confirmed the dose-dependent SARS-CoV-2 suppression in Vero E6 cells, with SAR405 exhibiting the highest SI. This superior profile aligned with SAR405's potent enzymatic inhibition (VPS34-IN-I: 25 nmol/L, VPS34-IN-II: 2 nmol/L, PIK-III: 18 nmol/L, SAR405:1.2 nmol/L)[30-33], establishing it as the most promising anti-coronavirus candidate among the tested VPS34-targeting compounds. This aligns with recent findings that VPS34

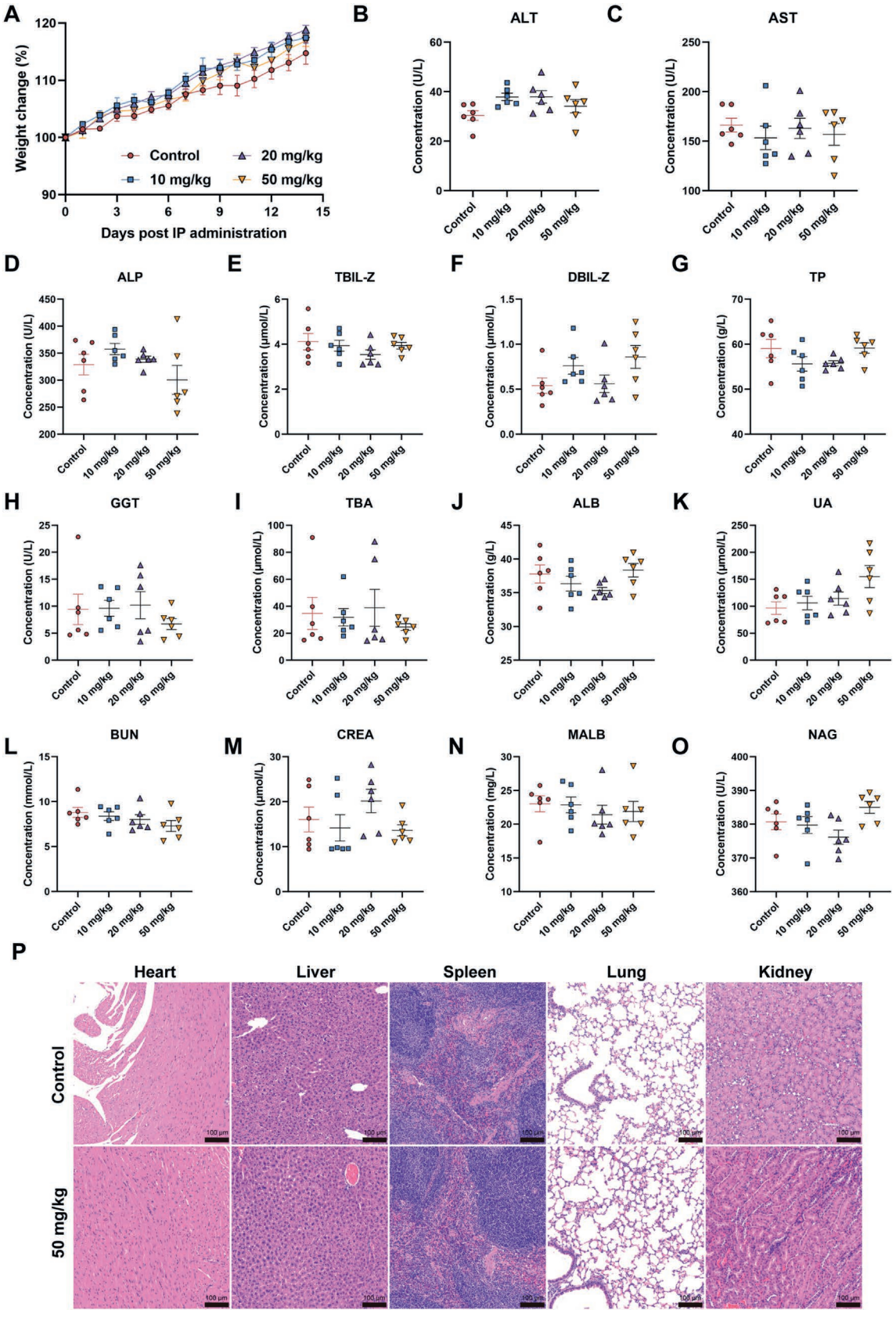


**Figure 8** The safety assessment of YBM *in vivo*. (A) Mice were intraperitoneally administered YBM (10, 20, and 50 mg/kg) or vehicle control daily for 14 consecutive days. Body weight monitoring throughout the dosing period. (B−O) Serum biochemical analysis of hepatic and renal function parameters. (P) Representative hematoxylin and eosin (H&E)-stained sections of heart, liver, spleen, lung, and kidney tissues.

inhibitors suppress SARS-CoV-2 replication in a human airway epithelial cell line and human lung tissues[46,47]. Compared to direct-acting antivirals (such as Paxlovid™), host-targeting strategies against VPS34 offer two key advantages: first, the high genetic barrier to resistance host proteins is less prone to mutation-driven drug resistance; second, broad-spectrum antiviral activity against emerging variants, as evidenced by comparable $EC_{50}$ values across all tested strains (Fig. 3C−F).

Paradoxically, SAR405 failed to confer protection in a lethal SARS-CoV-2 mouse model, despite its cellular efficacy (Fig. 4). SAR405's lack of *in vivo* efficacy stems not from intrinsic antiviral incompetence, but rather from inadequate spatiotemporal coordination between compound availability and pathogenic vulnerability windows. The compromised *in vivo* efficacy of SAR405 directly correlates with its suboptimal PK profile, characterized by rapid systemic clearance (3250.94 ± 1081.29 mL/h/kg) and transient target tissue exposure (Supporting Information Tables S2 and S3). Despite achieving peak plasma concentrations within 10 min post-administration, the compound demonstrated inadequate biodistribution to SARS-CoV-2 replication sites, with lung and tracheal concentrations remaining at a low level. This PK/PD disconnection, exacerbated by a short elimination half-life, mechanistically explains the absence of observable antiviral activity in murine infection models.

The rational optimization of PK profiles is a promising strategy for enhancing the therapeutic potential of antiviral agents. By improving critical PK parameters such as bioavailability, tissue distribution, and metabolic stability, this approach enables sustained target engagement at viral replication sites while minimizing off-target toxicity. For example, the modified analogs of tenofovir, azidothymidine, stavudine, and didanosine exhibit enhanced bioavailability, improved PK profile, increased cell permeability, and strong anti-HIV activity[48-50]. Lipid-based remdesivir prodrugs have been synthesized and evaluated in multiple studies, demonstrating high antiviral activity against SARS-CoV-2, oral bioavailability, and favorable PK profiles[51-53]. Through systematic structural modifications of the VPS34 inhibitor SAR405, we developed three novel compounds: YDT, YBT, and YBM. Strikingly, YBM exhibited superior PK properties conducive to *in vivo* antiviral activity compared with SAR405, while demonstrating significant therapeutic efficacy against lethal-dose SARS-CoV-2 and HCoV-OC43 infection *in vivo*. PK profiling revealed that YBM achieved 2.5-fold higher peak plasma concentration and 5-fold lower systemic clearance post-IP administration. This prolonged PK profile enables sustained VPS34 inhibition throughout the viral replication cycle. Crucially, YBM demonstrated enhanced lung tropism and maintained pulmonary drug concentrations higher than SAR405 at critical time points. This preferential pulmonary distribution ensures therapeutic coverage at the primary coronavirus replication site, which is a key determinant of antiviral success.

Although YBM ($K_D$: $2.19 \times 10^{-8}$ mol/L) has a reduced affinity for VPS34 compared with SAR405 ($K_D$: $1.44 \times 10^{-9}$ mol/L) (Supporting Information Fig. S8), it exhibits significantly improved pharmacokinetic properties. This apparent contradiction can be explained by considering the overall drug optimization process. The structural modifications in YBM, while slightly reducing static binding affinity in a purified system, were decisively successful in mitigating the primary liability of SAR405: its rapid metabolic clearance. We posit that in the complex physiological environment, the greatly improved metabolic stability and PK profile of YBM lead to higher and more sustained drug concentrations. This effectively compensates for the modestly lower intrinsic affinity, resulting in superior overall target coverage and efficacy *in vivo*. In drug discovery, the goal is not to optimize a single parameter (like $K_D$) in isolation, but to achieve the best possible balance of multiple properties—including potency, PK, and safety—to yield a successful therapeutic candidate. Our data demonstrate that YBM represents such a balanced candidate.

Thus, we validated VPS34 as a viable broad-spectrum anti-coronavirus target both *in vitro* and *in vivo*, and developed YBM, a novel VPS34-targeting compound that demonstrates favorable antiviral activity *in vivo*. YBM effectively inhibited not only $\beta$-coronaviruses but also $\alpha$-coronavirus and $\gamma$-coronavirus underscores its potential as a pan-coronavirus therapeutic. While our study demonstrated the safety of YBM following 14-day continuous administration, prolonged autophagic activation may still cause organismal damage[54]. Therefore, future studies should develop inhalation delivery systems to maximize bioavailability while minimizing systemic exposure. In addition, combination therapies using viral polymerase inhibitors should be explored to achieve synergistic effects[55].

## 5. Conclusions

In conclusion, our results show that VPS34 serves as a broad-spectrum host target for coronaviruses. A novel VPS34-targeting small-molecule compound was designed and synthesized, which exhibited favorable bioavailability and lung tissue distribution. This compound effectively inhibited coronavirus replication both *in vitro* and *in vivo* and holds promise for future structural optimization or combination therapy with viral polymerase inhibitors as broad-spectrum anti-coronavirus agents.

## Acknowledgments

This research was supported by the Jilin Province Science and Technology Development Plan Youth Growth Science and Technology Project (20230508167RC, China). We express our gratitude for the graphical abstract provided by BioRender.

## Author contributions

Chenchen Ge, Zihao Wang: Writing-review & editing, Writing-original draft, Software, Methodology, Formal analysis, Visualization, Data curation. Zhiwei Zhao, Xiaoyu Zhang, Xiaoyang Yu, Minghua Chen, Kai Liu, Lisen Lin, Dapeng Li, Ningyi Jin: Resource. Peifu Jiao, Shiyong Fan, Chao Shang: Writing-review & editing, Formal analysis, Data curation. Xiao Li: Supervision, Project administration, Funding acquisition. All authors contributed to the article and approved the submitted version.

## Conflicts of interest

The authors declare no conflicts of interest.

## Appendix A. Supporting information

Supporting information to this article can be found online at https://doi.org/10.1016/j.apsb.2025.12.020.

## References


1. World Health O. *COVID-19 epidemiological update, edition 177*. 12 March 2025. Available from: https://iris.who.int/handle/10665/380910.
2. WHO. Number of COVID-19 cases reported to WHO (cumulative total). Available from: https://data.who.int/dashboards/covid19/cases. (Accessed 30.3).
3. Macedo A, Gonçalves N, Febra C. COVID-19 fatality rates in hospitalized patients: systematic review and meta-analysis. *Ann Epidemiol* 2021;**57**:14−21.
4. Richardson S, Hirsch JS, Narasimhan M, Crawford JM, McGinn T, Davidson KW, et al. Presenting characteristics, comorbidities, and outcomes among 5700 patients hospitalized with COVID-19 in the New York City area. *JAMA* 2020;**323**:2052−9.
5. Msemburi W, Karlinsky A, Knutson V, Aleshin-Guendel S, Chatterji S, Wakefield J. The WHO estimates of excess mortality associated with the COVID-19 pandemic. *Nature* 2023;**613**:130−7.
6. Bian H, Chen L, Zhang Z, Wen AD, Zheng ZH, Song LQ, et al. Meplazumab, a CD147 antibody, for severe COVID-19: a double-blind, randomized, placebo-controlled, phase 3 clinical trial. *Signal Transduct Targeted Ther* 2025;**10**:119.
7. Owen DR, Allerton CMN, Anderson AS, Aschenbrenner L, Avery M, Berritt S, et al. An oral SARS-CoV-2 M(pro) inhibitor clinical candidate for the treatment of COVID-19. *Science* 2021;**374**:1586−93.
8. Zhou Y, Gammeltoft KA, Ryberg LA, Pham LV, Tjørnelund HD, Binderup A, et al. Nirmatrelvir-resistant SARS-CoV-2 variants with high fitness in an infectious cell culture system. *Sci Adv* 2022;**8**:eadd7197.
9. Zhu Y, Yurgelonis I, Noell S, Yang Q, Guan S, Li Z, et al. *In vitro* selection and analysis of SARS-CoV-2 nirmatrelvir resistance mutations contributing to clinical virus resistance surveillance. *Sci Adv* 2024;**10**:eadl4013.
10. Stevens LJ, Pruijssers AJ, Lee HW, Gordon CJ, Tchesnokov EP, Gribble J, et al. Mutations in the SARS-CoV-2 RNA-dependent RNA polymerase confer resistance to remdesivir by distinct mechanisms. *Sci Transl Med* 2022;**14**:eabo0718.
11. Gandhi S, Klein J, Robertson AJ, Peña-Hernández MA, Lin MJ, Roychoudhury P, et al. *De novo* emergence of a remdesivir resistance mutation during treatment of persistent SARS-CoV-2 infection in an immunocompromised patient: a case report. *Nat Commun* 2022;**13**:1547.
12. Hirotsu Y, Kobayashi H, Kakizaki Y, Saito A, Tsutsui T, Kawaguchi M, et al. Multidrug-resistant mutations to antiviral and antibody therapy in an immunocompromised patient infected with SARS-CoV-2. *Med* 2023;**4**:813-24.e4.
13. Xiong R, Zhang L, Li S, Sun Y, Ding M, Wang Y, et al. Novel and potent inhibitors targeting DHODH are broad-spectrum antivirals against RNA viruses including newly-emerged coronavirus SARS-CoV-2. *Protein Cell* 2020;**11**:723−39.
14. He Y, Zhou J, Gao H, Liu C, Zhan P, Liu X. Broad-spectrum antiviral strategy: host-targeting antivirals against emerging and re-emerging viruses. *Eur J Med Chem* 2024;**265**:116069.
15. Miller K, McGrath ME, Hu Z, Ariannejad S, Weston S, Frieman M, et al. Coronavirus interactions with the cellular autophagy machinery. *Autophagy* 2020;**16**:2131−9.
16. Reidick C, Boutouja F, Platta HW. The class III phosphatidylinositol 3-kinase Vps34 in *Saccharomyces cerevisiae*. *Biol Chem* 2017;**398**:677−85.
17. Levine B, Liu R, Dong X, Zhong Q. Beclin orthologs: integrative hubs of cell signaling, membrane trafficking, and physiology. *Trends Cell Biol* 2015;**25**:533−44.
18. Twu WI, Lee JY, Kim H, Prasad V, Cerikan B, Haselmann U, et al. Contribution of autophagy machinery factors to HCV and SARS-CoV-2 replication organelle formation. *Cell Rep* 2021;**37**:110049.
19. Shang C, Zhuang X, Zhang H, Li Y, Zhu Y, Lu J, et al. Inhibition of autophagy suppresses SARS-CoV-2 replication and ameliorates pneumonia in hACE2 transgenic mice and xenografted human lung tissues. *J Virol* 2021;**95**:e0153721.
20. Geraghty RJ, Aliota MT, Bonnac LF. Broad-spectrum antiviral strategies and nucleoside analogues. *Viruses* 2021;**13**:667.
21. Noman MZ, Parpal S, Van Moer K, Xiao M, Yu Y, Viklund J, et al. Inhibition of Vps34 reprograms cold into hot inflamed tumors and improves anti-PD-1/PD-L1 immunotherapy. *Sci Adv* 2020;**6**:eaax7881.
22. Feng S, Fan Z, Zhou K, Ma S, Liang M, Zhang H, et al. Subunit vaccine raised against the SARS-CoV-2 spike of Delta and Omicron variants. *J Med Virol* 2023;**95**:e29160.
23. Xu T, Li K, Huang S, Ivanov KI, Yang S, Ji Y, et al. Anti-SARS-CoV-2 prodrug ATV006 has broad-spectrum antiviral activity against human and animal coronaviruses. *Acta Pharm Sin B* 2025;**15**:2498−510.
24. Zhang M, Wang C, Feng L, Yang Q, Cao Y, Zhao Y, et al. Targeting SARS-CoV-2 main protease for the discovery of a broad-spectrum COVID-19 inhibitor by intensive multi-tiered validation. *Acta Pharm Sin B* 2025;**15**:5789−802.
25. Ricciardi S, Guarino AM, Giaquinto L, Polishchuk EV, Santoro M, Di Tullio G, et al. The role of NSP6 in the biogenesis of the SARS-CoV-2 replication organelle. *Nature* 2022;**606**:761−8.
26. Knoops K, Kikkert M, Worm SH, Zevenhoven-Dobbe JC, van der Meer Y, Koster AJ, et al. SARS-coronavirus replication is supported by a reticulovesicular network of modified endoplasmic reticulum. *PLoS Biol* 2008;**6**:e226.
27. Yan F, Li E, Wang T, Li Y, Liu J, Wang W, et al. Characterization of two heterogeneous lethal mouse-adapted SARS-CoV-2 variants recapitulating representative aspects of human COVID-19. *Front Immunol* 2022;**13**:821664.
28. Luo R, Shen B, Qian B, Fan L, Zhang J, Deng X, et al. Taurultam shows antiviral activity against SARS-CoV-2 and influenza virus. *BMC Microbiol* 2025;**25**:292.
29. Reifler A, Li X, Archambeau AJ, McDade JR, Sabha N, Michele DE, et al. Conditional knockout of PIK3C3 causes a murine muscular dystrophy. *Am J Pathol* 2014;**184**:1819−30.
30. Bago R, Malik N, Munson MJ, Prescott AR, Davies P, Sommer E, et al. Characterization of VPS34-IN1, a selective inhibitor of Vps34, reveals that the phosphatidylinositol 3-phosphate-binding SGK3 protein kinase is a downstream target of class III phosphoinositide 3-kinase. *Biochem J* 2014;**463**:413−27.
31. Pasquier B, El-Ahmad Y, Filoche-Rommé B, Dureuil C, Fassy F, Abecassis PY, et al. Discovery of (2*S*)-8-[(3*R*)-3-methylmorpholin-4-yl]-1-(3-methyl-2-oxobutyl)-2-(trifluoromethyl)-3,4-dihydro-2*H*-pyrimido[1,2-*a*]pyrimidin-6-one: a novel potent and selective inhibitor of Vps34 for the treatment of solid tumors. *J Med Chem* 2015;**58**:376−400.
32. Dowdle WE, Nyfeler B, Nagel J, Elling RA, Liu S, Triantafellow E, et al. Selective VPS34 inhibitor blocks autophagy and uncovers a role for NCOA4 in ferritin degradation and iron homeostasis *in vivo*. *Nat Cell Biol* 2014;**16**:1069−79.
33. Ronan B, Flamand O, Vescovi L, Dureuil C, Durand L, Fassy F, et al. A highly potent and selective Vps34 inhibitor alters vesicle trafficking and autophagy. *Nat Chem Biol* 2014;**10**:1013−9.
34. Lee N, Hui D, Wu A, Chan P, Cameron P, Joynt GM, et al. A major outbreak of severe acute respiratory syndrome in Hong Kong. *N Engl J Med* 2003;**348**:1986−94.
35. de Groot RJ, Baker SC, Baric RS, Brown CS, Drosten C, Enjuanes L, et al. Middle East respiratory syndrome coronavirus (MERS-CoV): announcement of the Coronavirus Study Group. *J Virol* 2013;**87**:7790−2.
36. Zaki AM, van Boheemen S, Bestebroer TM, Osterhaus AD, Fouchier RA. Isolation of a novel coronavirus from a man with pneumonia in Saudi Arabia. *N Engl J Med* 2012;**367**:1814−20.
37. Hu B, Guo H, Zhou P, Shi ZL. Characteristics of SARS-CoV-2 and COVID-19. *Nat Rev Microbiol* 2021;**19**:141−54.
38. Jayk Bernal A, Gomes da Silva MM, Musungaie DB, Kovalchuk E, Gonzalez A, Delos Reyes V, et al. Molnupiravir for oral treatment of COVID-19 in nonhospitalized patients. *N Engl J Med* 2022;**386**:509−20.

39. Backer JM. The intricate regulation and complex functions of the Class III phosphoinositide 3-kinase Vps34. *Biochem J* 2016;**473**: 2251−71.
40. Ohashi Y, Tremel S, Masson GR, McGinney L, Boulanger J, Rostislavleva K, et al. Membrane characteristics tune activities of endosomal and autophagic human VPS34 complexes. *eLife* 2020;**9**: e58281.
41. Feng Z, Xu K, Kovalev N, Nagy PD. Recruitment of Vps34 PI3K and enrichment of PI3P phosphoinositide in the viral replication compartment is crucial for replication of a positive-strand RNA virus. *PLoS Pathog* 2019;**15**:e1007530.
42. Gong M, Peng C, Yang C, Wang Z, Qian H, Hu X, et al. Genome-wide CRISPR/Cas9 screen identifies SLC39A9 and PIK3C3 as crucial entry factors for Ebola virus infection. *PLoS Pathog* 2024;**20**:e1012444.
43. Baggen J, Persoons L, Vanstreels E, Jansen S, Van Looveren D, Boeckx B, et al. Genome-wide CRISPR screening identifies TMEM106B as a proviral host factor for SARS-CoV-2. *Nat Genet* 2021;**53**:435−44.
44. Daniloski Z, Jordan TX, Wessels HH, Hoagland DA, Kasela S, Legut M, et al. Identification of required host factors for SARS-CoV-2 infection in human cells. *Cell* 2021;**184**:92−105.e16.
45. Wang R, Simoneau CR, Kulsuptrakul J, Bouhaddou M, Travisano KA, Hayashi JM, et al. Genetic screens identify host factors for SARS-CoV-2 and common cold coronaviruses. *Cell* 2021;**184**:106-19.e14.
46. Williams CG, Jureka AS, Silvas JA, Nicolini AM, Chvatal SA, Carlson-Stevermer J, et al. Inhibitors of VPS34 and fatty-acid metabolism suppress SARS-CoV-2 replication. *Cell Rep* 2021;**36**:109479.
47. Yuen CK, Wong WM, Mak LF, Wang X, Chu H, Yuen KY, et al. Suppression of SARS-CoV-2 infection in *ex-vivo* human lung tissues by targeting class III phosphoinositide 3-kinase. *J Med Virol* 2021;**93**: 2076−83.
48. Durand-Gasselin L, Van Rompay KK, Vela JE, Henne IN, Lee WA, Rhodes GR, et al. Nucleotide analogue prodrug tenofovir disoproxil enhances lymphoid cell loading following oral administration in monkeys. *Mol Pharm* 2009;**6**:1145−51.
49. Hong X, Cai Z, Zhou F, Jin X, Wang G, Ouyang B, et al. Improved pharmacokinetics of tenofovir ester prodrugs strengthened the inhibition of HBV replication and the rebalance of hepatocellular metabolism in preclinical models. *Front Pharmacol* 2022;**13**:932934.
50. Zhang Y, Gao Y, Wen X, Ma H. Current prodrug strategies for improving oral absorption of nucleoside analogues. *Asian J Pharm Sci* 2014;**9**:65−74.
51. El-Sayed NS, Jureka AS, Edwards MR, Lohan S, Williams CG, Keiser PT, et al. Synthesis and antiviral activity of fatty acyl conjugates of remdesivir against severe acute respiratory syndrome coronavirus 2 and Ebola virus. *Eur J Med Chem* 2021;**226**:113862.
52. Hu H, Mady Traore MD, Li R, Yuan H, He M, Wen B, et al. Optimization of the prodrug moiety of Remdesivir to improve lung exposure/selectivity and enhance anti-SARS-CoV-2 activity. *J Med Chem* 2022;**65**:12044−54.
53. Schooley RT, Carlin AF, Beadle JR, Valiaeva N, Zhang XQ, Clark AE, et al. Rethinking Remdesivir: synthesis, antiviral activity, and pharmacokinetics of oral lipid prodrugs. *Antimicrob Agents Chemother* 2021;**65**:e0115521.
54. Kim KH, Lee MS. Autophagy−a key player in cellular and body metabolism. *Nat Rev Endocrinol* 2014;**10**:322−37.
55. Shan H, Zhou Y, Qin Y, Guo T, Zhang X, Xiang H, et al. Discovery of SARS-CoV-2 PLpro inhibitors and RIPK1 inhibitors with synergistic antiviral efficacy in a mouse COVID-19 model. *Acta Pharm Sin B* 2025. Available from: https://doi.org/10.1016/j.apsb.2025.09.026.